Hindawi
International Journal of Intelligent Systems
Volume 2023, Article ID 4506331, 17 pages
https://doi.org/10.1155/2023/4506331

WILEY | Hindawi

Research Article

Two-Step Unsupervised Approach for Sand-Dust Image Enhancement

Guxue Gao,[1,2] **Huicheng Lai**,[1,2] **and Zhenhong Jia**[1,2]

[1]*College of Information Science and Engineering, Xinjiang University, Urumqi 830017, China*
[2]*Key Laboratory of Signal Detection and Processing, Xinjiang University, Urumqi 830017, China*

Correspondence should be addressed to Huicheng Lai; lai@xju.edu.cn

Received 12 December 2022; Revised 19 March 2023; Accepted 25 April 2023; Published 13 May 2023

Academic Editor: Surya Prakash

In sand-dust environments, light is scattered and absorbed, and sand-dust images thus suffer from severe image degradation problems, such as color shifts, low contrast, and blurred details. To address these problems, we propose a two-step unsupervised sand-dust image enhancement algorithm. In the first step, a convenient and competent color correction method is put forward to solve the color shift problem. Considering the wavelength attenuation features of sand-dust images, a linear stretching and blue channel compensation method is designed, and an adaptive color shift correction factor is developed to remove the color shift. In the second step, to enhance the clarity and details of the images, an unsupervised generative adversarial network is proposed, which does not require pairs of data for training. To reduce detail loss, the detail enhancement branch is designed, and the generator considers to more details through the constructed coarse-grained and fine-grained discriminators. The introduced multiscale perceptual loss promotes the image fidelity well. Experiments show that the proposed method achieves better color correction, enhances image details and clarity, has a better subjective effect, and outperforms existing sand-dust image enhancement methods both quantitatively and qualitatively. Similarly, our method promotes the application capability of the target detection algorithm and also has a good enhancement effect on underwater images and haze images.

1. Introduction

In sand-dust environments, the atmosphere is filled with many sand-dust particles, which seriously degrades the images captured by outdoor devices. This issue manifests in such images as color shifts, low contrast, and blurred details, and even severe noise. Sand-dust-degraded images hinder the ability to obtain valuable information and severely degrade the ability to run subsequent advanced tasks such as scene understanding [1], object recognition [2], and video surveillance [3]. Therefore, it is necessary and meaningful to develop an image dedusting algorithm to obtain high-quality clear images without sand dust. Such a method would promote the intelligent application of computer vision.

Existing image dedusting algorithms are not ideal in terms of color restoration and detail preservation. In terms of color restoration, most color correction algorithms ignore the features of the wavelength attenuation of dust images and the cause of color shift; thus, when applied to sand-dust images, color distortions occur. Image detail preservation is primarily based on two mainstream technologies: image enhancement technology and the image formation model. These two methods restore the details of the image to some extent but cause other problems, and the resulting image visibility is poor. Deep learning methods obtain better results, but most require training paired data.

Because paired sand-dust datasets are difficult to obtain, even if they can be synthesized by certain methods, the generalizability of such methods to real scenes is weak due to the gap between them and the real domain. To our knowledge, few researchers have enhanced the details of sand-dust images through unpaired methods of deep learning. Inspired by image translation [4], we use generative adversarial networks (GAN) to address the details of sand-dust images and build an unpaired mapping between blurred image space and clear image space, which reduces

the dependence on paired sand-dust datasets. We introduce a one-path GAN, and unlike [4, 5], we do not need to use cycle-consistency and two-way GANs. Training the network is difficult due to the scarcity of paired training data; thus, we make certain improvements to the proposed method. To reduce detail loss, we design a detail enhancement branch, and there is no real label during training. We also introduce a multiscale perceptual function to reduce the content deviation and guide the generator to focus on more image details by the designed coarse-grained and fine-grained discriminators.

We propose a two-step unsupervised sand-dust image enhancement (SIE) algorithm. The method can be decomposed into two processes: color correction and detail refinement. A color correction method is first designed based on the property of wavelength attenuation of sand-dust images. To enhance the contrast and details of the images, we propose an unsupervised method to enhance the sand-dust images. The visualization is shown in Figure 1, and the specific primary contributions are summarized as follows:

(1) A convenient and competent color correction method is proposed. The method is designed with a linear stretch, blue channel compensation, and color shift removal to achieve color correction.

(2) We design an unsupervised generative adversarial network to refine the image's details. The unsupervised network reduces the detail loss by designing a detail enhancement branch and guides the generator to focus on more details by constructing coarse-grained and fine-grained discriminators. The multiscale perceptual function is introduced to improve the image fidelity.

(3) Experiments show that the method exhibits the obvious advantages of high clarity and clear details. In addition, the proposed method promotes the application capability of the target detection algorithm and is also suitable for other degraded images.

2. Related Works

2.1. Traditional Methods. Traditional methods primarily include image enhancement and image formation models. Image enhancement methods are primarily used to achieve a specific purpose by processing and transforming image pixel values. This type of method is common in image dehazing [6], low-light image enhancement [7], and other fields. Specifically, in image dedusting, Al Ameen et al. [8] introduced fuzzy operators to process dust images. Although the image's sharpness is improved, the color shift problem is still prominent. Fu et al. [9] designed a fusion method that performs color correction and detail enhancement through a statistical strategy and fusion of images with different luminances derived from the gamma function; however, severe dust images cannot be processed effectively. Gao et al. [10] removed the dust through the YUV space. In the space, the method achieves color correction by color components U and V and enhances the contrast by processing the luminance component Y. However, there is still sand dust in some areas of the sky. Park and Eom [11] used the designed color balance and histogram to enhance the sand-dust image. Good results are achieved in detail enhancement and color restoration. However, the image's tone is cold, which introduces considerable noise during enhancement. Xu et al. [12] proposed the least square sand-dust image model. These image enhancement methods enhance the image detail information to some extent, but the subjective visual effect is poor, and there are problems of color distortion and noise.

The image formation model method is primarily used to establish an approximate mathematical relationship by analyzing the causes of image degradation. Gao et al. [13] developed a method of reversing the blue channel to restore the image. This method achieved good detail enhancement and color correction using prior information and integrated the factor into the image formation model. However, with severely distorted sand-dust images, this prior information was insufficient, resulting in color distortion. Kim et al. [14] derived the scene transfer function by saturation and combined it with a white balance technique to remove sand-dust. This method was not robust and could not manage most sand-dust images. Dhara et al. [15] improved the dark channel and estimated accurate atmospheric light to recover the sand-dust image. This improved method cannot eliminate the color shift and improve the image visibility. Yang et al. [16] used the histogram matching method to remove color bias and improved image clarity through the optimized atmospheric scattering model, but the sky region was prone to halo. Similar methods were also used in [17, 18]. These methods based on image formation models cause color distortions when encountering images with complex scenes, which affect the overall visual effect. Thus, the robustness of these methods must be improved.

2.2. Deep Learning Methods. Based on paired data, image dehazing [19, 20], image deraining [21], and low-light image enhancement [22] have achieved good results. However, deep learning methods have not been well studied in image dedusting, primarily due to the limitation of the dataset. Recently, the sand-dust images were synthesized by Si et al. [23], who conducted quantitative and qualitative evaluations of the synthesized images. However, compared with the real sand-dust image, the synthetic sand-dust image still has a big gap. Huang et al. [24] developed a new loss function and designed a network model with dust extraction and color correction for image desanding. This method has achieved certain results in real scenes but produces color distortion and insufficient definition. Huang et al. [25] developed a network model for image desanding by using several dilated convolution residual blocks and designed weighting modules. Affected by the synthetic dataset, this method achieves better performance on synthetic datasets but is not ideal in real scenarios. Liang et al. [26] remove sand-dust based on color correction and dehazing network. This method uses a similar dehazing method to process the image after color correction and unwraps the model parameters

(a) (b)

Figure 1: Visualization examples. (a) Sand-dust images and (b) our results.

through an unsupervised network. However, the image recovered by this method is prone to color distortion.

2.3. Unsupervised Learning. Initially, unsupervised generative adversarial networks [4] achieved good results in the field of image translation. With subsequent developments, unsupervised learning has been extended and applied to other tasks. Recently, [27–30] have achieved good results in image deblurring, image denoising, image dehazing, and image deraining. Because unsupervised training is not supervised by ground truth images, [29, 30] used a two-way GAN with a joint loss function to constrain the network training. References [31, 32] tried to use a single generative adversarial network for aesthetic image and low-light image enhancement. To train the network effectively, they designed an attention module with some prior knowledge and combined multiple loss functions to constrain the network. Unlike these tasks, we use a one-way generation adversarial network to refine the image details and improve the single generation adversarial network to adapt to the task of interest. To reduce detail loss, we design a detail enhancement branch. To guide the generator to focus on more details, we design coarse-grained and fine-grained discriminators and constrain the network well with a multiscale perceptual function.

3. Proposed Method

We propose a two-step unsupervised SIE method, including an adaptive color correction module and an unsupervised detail refinement network module. Details are shown in Figure 2. The technical details of the proposed modules are described in terms of these two aspects.

3.1. Adaptive Color Correction Model. Under sand-dust conditions, images have serious color shifts due to the influence of the medium during the propagation of light. Most sand-dust images are yellow or red, which affects their visual appeal. Therefore, such color correction algorithms need to be developed urgently. Some traditional color correction algorithms, such as the Gray World algorithm [33], Gray Edge [34], Shades of Gray [35], and Max RGB [36], implement color correction by relying on specific assumptions. However, the specific assumptions in these algorithms are not tailored for sand-dust images; thus, it is inappropriate to correct the sand-dust images. Unlike these algorithms, we specifically study the sand-dust image and explore the cause of color shift by analyzing the wavelength attenuation characteristics in Figure 3 to achieve color correction. Compared with the wavelength attenuation of clear images, it has the following characteristics: (a) the dynamic range is narrow; (b) the blue channel's attenuation is more severe than the other two channels; and (c) the deviation of the three channels is larger. Thus, we design an adaptive color correction strategy (i.e., red-green channel stretch-compensation-blue channel stretch-color shift removal). Considering (a) and (b) above, to extend the pixel-level distribution, the red and green channels are first stretched, with formulae (1) and (2). Due to the serious attenuation of the blue channel, direct stretching will cause excessive color correction. Therefore, a method of compensating blue channel is designed, which compensates by selecting well-preserved green channel, with the aim of reducing blue artifacts and distortions. The relevant formula is shown in (3), and the compensated blue channel is stretched to the entire pixel level, as shown in (4):

$$I_s^r = 255 * \frac{\left(I^r - I_{\min}^r\right)}{\left(I_{\max}^r - I_{\min}^r\right)}, \tag{1}$$

$$I_s^g = 255 * \frac{\left(I^g - I_{\min}^g\right)}{\left(I_{\max}^g - I_{\min}^g\right)}, \tag{2}$$

$$I_c^b = I^b + \alpha * \left(I_{s-\text{mean}}^g - I_{\text{mean}}^b\right) * I_s^g, \tag{3}$$

$$I_s^b = 255 * \frac{\left(I_c^b - I_{c-\min}^b\right)}{\left(I_{c-\max}^b - I_{c-\min}^b\right)}, \tag{4}$$

where I_s^r, I_s^g, and I_s^b refer to the RGB channels after stretching, respectively; I^r, I^g, and I^b represent the RGB channels of the input image, respectively; $I_{\max}^r$ and $I_{\min}^r$ refer to the maximum and minimum values of the input image's red channel, respectively; similarly, the meaning of $I_{\max}^g$ and $I_{\min}^g$ can be derived; $I_{s-\text{mean}}^g$ is the blue channel's mean value after stretching; I_{mean}^b is the blue channel's mean value of the input image; I_c^b is the blue channel after compensation; α is

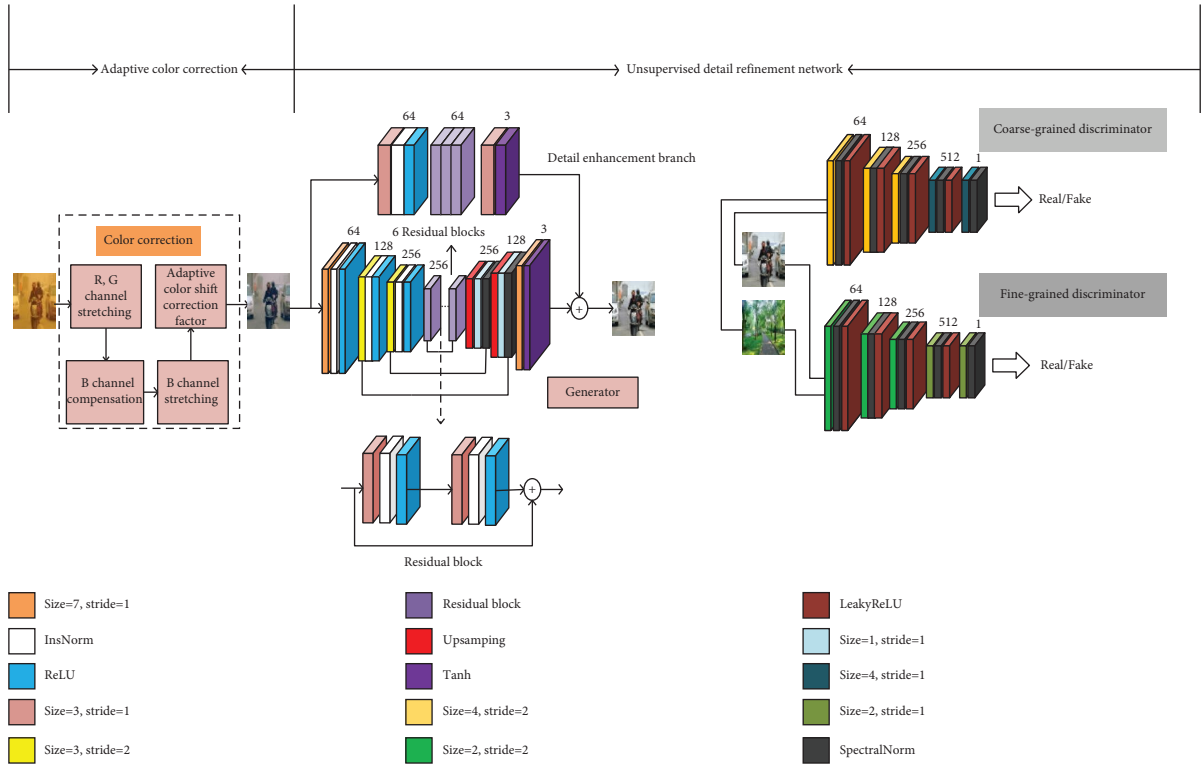

Figure 2: Proposed unsupervised SIE framework, where the size in the icon refers to the convolution kernel size, and R, G, and B represent the red, green, and blue channels, respectively.

the compensation gain coefficient; and $I^b_{c-\max}$ and $I^b_{c-\min}$ are the maximum and minimum values of the blue channel after compensation, respectively. After these operations, there is a deviation in the wavelength distribution of the three channels, resulting in color shifts. Considering the characteristic c of the sand-dust image, we adjust each channel by the color shift correction factor. Taking the information of the green channel as a reference, we adjust the other two channels so that the three-channel wavelength has a similar distribution; the specific formulae are as follows:

$$I^r_{\text{final}} = I^r_s + \beta * \left(I^g_{s-\text{mean}} - I^r_{s-\text{mean}}\right), \tag{5}$$

$$I^b_{\text{final}} = I^b_s + \beta * \left(I^g_{s-\text{mean}} - I^b_{s-\text{mean}}\right), \tag{6}$$

where $I^r_{s-\text{mean}}$, $I^g_{s-\text{mean}}$, and $I^b_{s-\text{mean}}$ are the mean values of the RGB channels after stretching, respectively; β is the color shift adjustment coefficient; and I^r_{final} and I^b_{final} are the final color correction's red channel and blue channel. The entire color correction process is shown on the left in Figure 2. The image corrected by the above formulae and the corresponding wavelength attenuation maps are shown in Figures 4 and 5. Figures 4 and 5(g) show that the pixel range is well extended to the entire pixel level after the stretching operation for the red and green channels. As shown in Figures 4 and 5(h), after the compensation operation, the blue channel is effectively compensated, but the pixel-level distribution is not balanced, and the blue channel must be further adjusted. As shown in the histogram distribution in Figures 4 and 5(i), the range of pixels is adjusted by stretching the blue channel and then becoming balanced, which attenuates color distortion. Although the color shift is attenuated in Figures 4 and 5(d), there is a small amount of sand and dust. Through the corresponding wavelength distribution, there is also a marginal deviation in the distribution of the three channels. After the color shift factor adjustment, Figures 4 and 5(e) show natural colors, and the corresponding wavelength distribution is further fitted, showing a better color correction effect.

3.2. Unsupervised Detail Refinement Network. After color correction, the color shift is removed effectively, but image details are not sufficiently clear, the contrast is low, and the image must be further processed to improve its visibility. Thus, we propose an unsupervised detail refinement generative adversarial network, and the network structure is shown on the right side of Figure 2 and includes the generator structure and coarse-grained and fine-grained discriminator structures. The structures of the generator and discriminator and the loss functions used are described in detail.

3.2.1. Generator. We use a U-Net structure similar to [4] as the backbone of the generator, consisting of an encoder, a feature transformer, and a decoder. Figure 2 shows its structure. The encoder consists of a feature extraction unit and two downsampling units. The downsampling unit consists of a convolution with a stride of 2, a normalization function InsNorm, and an activation function ReLU. The

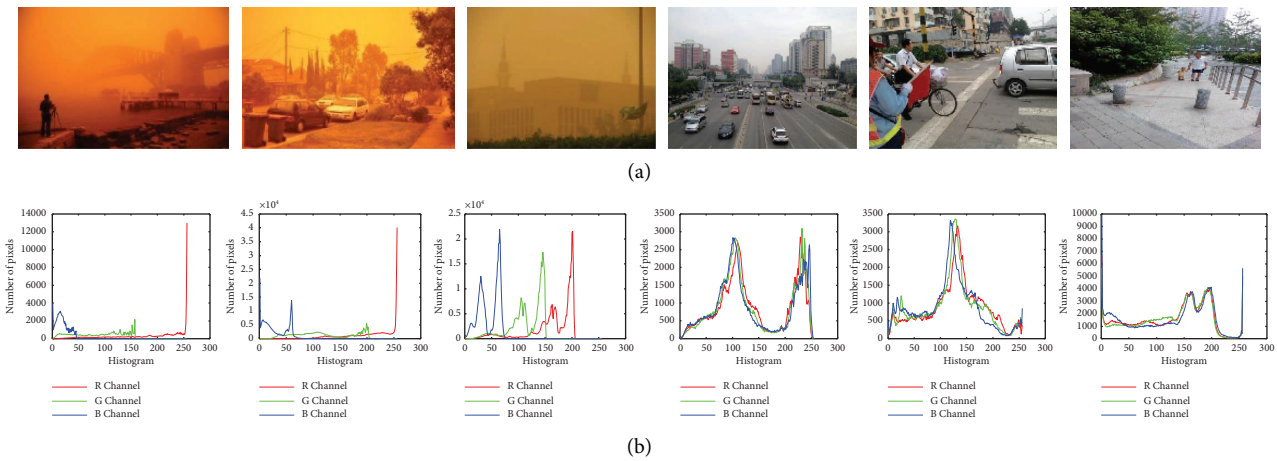

FIGURE 3: Images and the corresponding wavelength attenuation maps. (a) Sand-dust and clear images and (b) wavelength attenuation maps corresponding to (a).

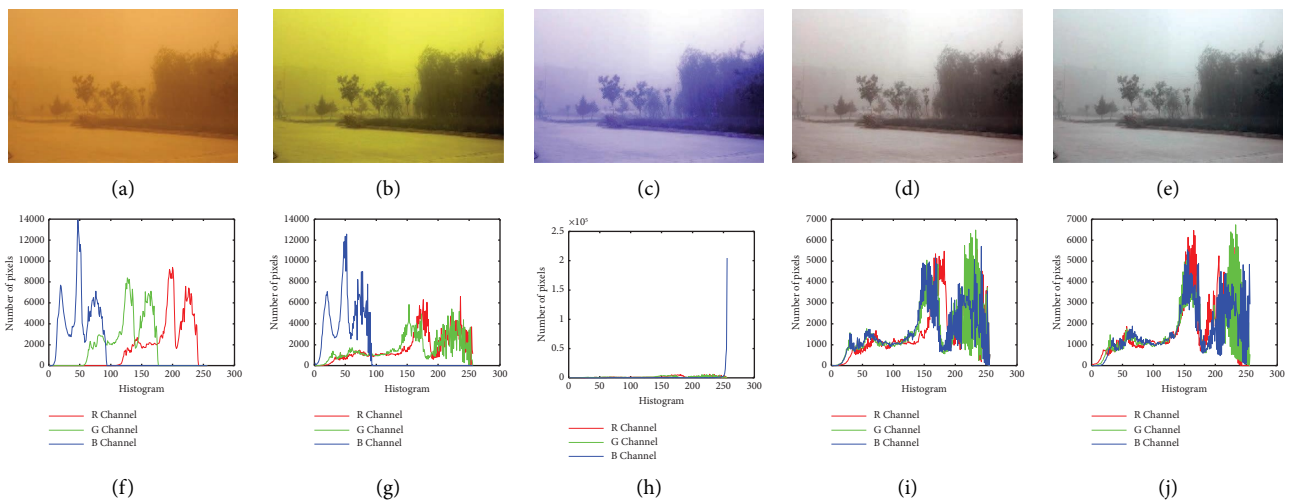

FIGURE 4: Color correction process and corresponding wavelength attenuation maps. (a) Sand-dust image, (b) red and green channel stretching, (c) blue channel compensation, (d) blue channel stretching, (e) color shift removal, and (f)–(j) are wavelength attenuation maps corresponding to (a)–(e), respectively.

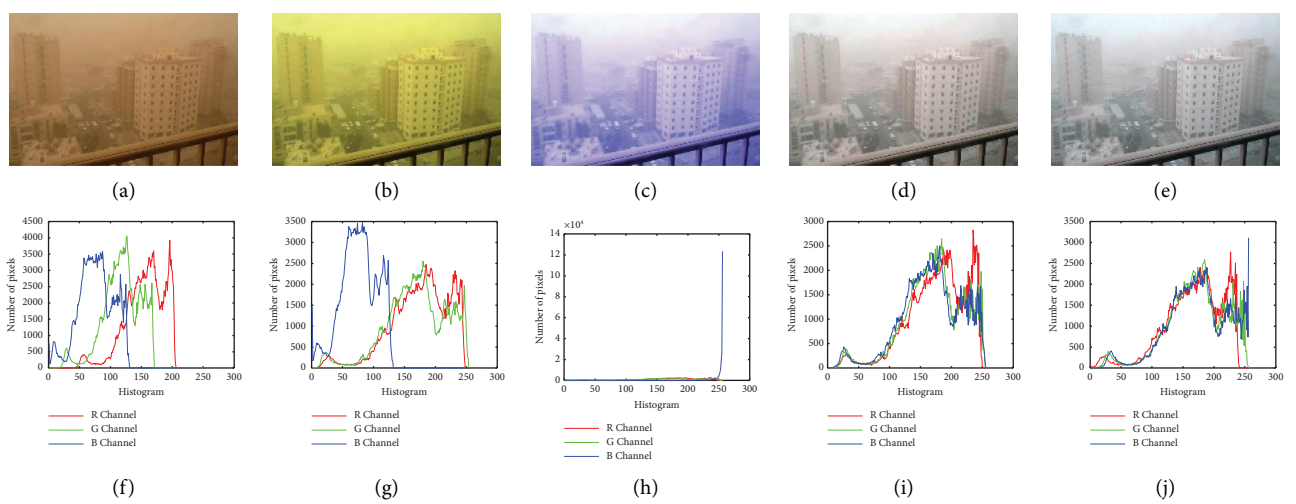

FIGURE 5: Color correction process and corresponding wavelength attenuation maps. (a) Sand-dust image, (b) red and green channel stretching, (c) blue channel compensation, (d) blue channel stretching, (e) color shift removal, and (f)–(j) are wavelength attenuation maps corresponding to (a)–(e), respectively.

feature transformer is composed of 6 identical residual blocks. The decoder consists of two upsampling units, followed by a feature enhancement module. In the upsampling unit of the decoder, we used a bilinear sampling layer and a $1 * 1$ convolution layer instead of the deconvolution operation used in [4] to reduce the checkerboard effect, followed by the spectral normalization function. The spectral normalization function has been shown to be stable in network training [37]. In addition, to make use of the shallow information, we also use the skip connection operation. Although encoder-decoder structures such as U-Net can extract deep semantic information, which is important for image representation, this upsampling and downsampling operation will result in the loss of details. Therefore, to retain more information, we design the detail enhancement branch, as shown in the upper part of Figure 2. This detail enhancement branch uses a full convolution operation, by which the detail loss can be effectively reduced.

3.2.2. Discriminator. The discriminator continuously guides the generator to produce more realistic images by discriminating between the real and generated images. Discriminators play an important role in generative adversarial training. In this study, we use the PatchGAN structure in [4] and introduce a spectral normalization function to increase the stability of training. Because PatchGAN uses a single-scale convolutional kernel $4 * 4$, this perceptual field limitation can only guide the generator to generate details at a global scale. This guidance is coarse-grained and cannot guide the generation of minute details. Thus, based on a coarse-grained discriminator, we propose a fine-grained discriminator. This fine-grained discriminator guides the generator to focus on local details by employing a small-scale $2 * 2$ convolution kernel. Its structure is shown on the right side of Figure 2. The constructed coarse-grained and fine-grained discriminators are experimentally verified to be effective in promoting the enhancement of more details.

3.2.3. Loss Function. The adversarial loss is exploited to fit the distribution between images. Least-square GAN (LSGAN) loss [38] can make the network training more stable, and we thus use LSGAN loss as the generative adversarial loss, and the formulae are as follows:

$$\begin{aligned} L_G &= E_{G(x)\sim p_{\text{fake}}}\left[D_C(G(x)-1)^2\right] \\ &\quad + E_{G(x)\sim p_{\text{fake}}}\left[D_F(G(x)-1)^2\right], \\ L_D &= E_{y\sim P_{\text{real}}}\left[(D_C(y)-1)^2\right] + E_{G(x)\sim P_{\text{fake}}}\left[\left(D_C(G(x))^2\right]\right. \\ &\quad + E_{y\sim P_{\text{real}}}\left[(D_F(y)-1)^2\right] + E_{G(x)\sim P_{\text{fake}}}\left[\left(D_F(G(x))^2\right]\right., \end{aligned} \tag{7}$$

where L_G is the adversarial loss of generator G; D_C and D_F are the coarse-grained discriminator and fine-grained discriminator, respectively; x is the image after color correction; y contains high-quality clear domain images; and L_D is the loss of discriminator D. Because the training is unpaired, there is no supervision of ground truth images. We also introduce a multiscale perceptual loss function that sends the generated and input images to a pretrained VGG19 network [39] and calculates their feature distances in feature space to reduce the bias of semantic features and enhance the image fidelity. The formula is as follows:

$$L_P = \sum_{i=1}^{I} \left\| \varphi_i(x) - \varphi_i(G(x))_2, \right. \tag{8}$$

where $\varphi_i(\cdot)$ is the feature map, which comes from the output of the i-th layer of the VGG19. In this study, we use the Relu_1_1, Relu_2_1, Relu_3_1, Relu_4_1, and Relu_5_1 layers to calculate the feature distance between the two images. $\|\cdot\|_2$ stands for the l_2 norm; I is the total number of layers; and L_P is the multiscale perceptual loss. Then, the total loss of the generator is

$$L = L_G + L_P. \tag{9}$$

4. Experimental Results and Analysis

4.1. Dataset and Application Details. Because no large sand-dust datasets are publicly available, we collected 700 sand-dust images and 1500 high-quality clear domain images to create a training set and train the generative adversarial network; the test set consists of 130 sand-dust images and 240 high-quality clear images, where 240 high-quality clear domain images are primarily used to calculate the Fréchet inception distance (FID) [40] with the recovered images. During network training and testing, the size of the input image is resized to $256 * 256$, and the network output image is in PNG format.

The color correction process was implemented in MATLAB with a computer with Intel(R) Core(TM) i7-8700 CPU @ 3.20 GHz, 16 GB RAM, and the network training model was implemented in PyTorch on an NVIDIA Tesla V100 GPU with 16 G of memory. ADAM is used as an optimizer for the generator and discriminator with a batch size of 1.200 epochs were trained. The first 100 epochs were run with a fixed learning rate of 0.0002, and the learning rate for the last 100 epochs decayed linearly to 0. In this study, α in formula (3) is equal to 5, and β in formula (5) is equal to 1.5.

4.2. Parameter Sensitivity Analysis. In the following, we explore the effect of α and β on the color correction. After several experiments, the color correction is shown to obtain better results when $\alpha = 5$ and $\beta = 1.5$. To verify the effect of α on color correction, we set $\beta = 1.5$ and explore the effect when α is equal to 1, 3, 5, and 7. Figure 6 shows that when $\alpha = 1$, blue artifacts occur; when $\alpha = 3$, blue artifacts decrease in frequency markedly; and when $\alpha = 5$ and 7, no artifacts occur. Therefore, we set $\alpha = 5$. To describe the effect of β on color correction, we set $\alpha = 5$ and explore the recovery effect when β equals 1, 1.5, 2, and 2.5. Figure 7 shows that when $\beta = 1$, the image has slight dust: when $\beta = 1.5$, the dust of the image is weakened, and the color is relatively normal; when $\beta = 2$ and 2.5, the image has a cyan tone. Therefore, we set $\beta = 1.5$ in this study.

(a) (b) (c) (d) (e)

Figure 6: Effect of α on color correction. (a) Sand-dust images, (b) color correction results for $\alpha = 1$, (c) color correction results for $\alpha = 3$, (d) color correction results for $\alpha = 5$, and (e) color correction results for $\alpha = 7$.

(a) (b) (c) (d) (e)

Figure 7: Effect of β on color correction. (a) Sand-dust images, (b) color correction results for $\beta = 1$, (c) color correction results for $\beta = 1.5$, (d) color correction results for $\beta = 2$, and (e) color correction results for $\beta = 2.5$.

4.3. Qualitative Evaluation

4.3.1. Qualitative Evaluation of Color Correction. For qualitative evaluation, we compare it with several other algorithms, including Gray Edge [34], Max RGB [36], Shades of Gray [35], Gray World [33], and OTM [16]. Figures 8 and 9 show that Gray Edge [34], Max RGB [36], and Shades of Gray [35] cannot remove the color shift. Although Gray-World [33] removes the color shift to some extent, it produces blue artifacts and color distortions in the color correction process because it does not consider the serious attenuation of the blue channel, while the image processed by OTM [16] is brighter, loses some details, and has color distortions in the foreground. The proposed algorithm removes the color shift well, does not introduce color distortions, and maintains image details, which is superior to other algorithms.

4.3.2. Qualitative Evaluation of the Sand-Dust Image Enhancement Effect. The visualization is more intuitive to reflect the recovery effect. Thus, we compare it with seven other sand-dust comparison algorithms (RDCP [18], CC [15], FSS [14], VR [16], RBCP [13], SES [11], and AOP [17]) and report visual recovery results in Figures 10 and 11. The source code is published by the author. Our code will be available at https://github.com/ggxzxc/Sand-dust-Image-Enhancement.

As shown in Figure 10, RDCP [18], VR [16], RBCP [13], and SES [11] perform well, while other comparison algorithms cannot effectively remove sand dust, and the resulting visibility is poor. RDCP [18] appears overenhanced, and the image is cool-toned. VR [16] has insufficient contrast. RBCP [13] shows color distortions, and SES [11] has a lot of noise. As shown in Figure 11, except for SES [11], all other

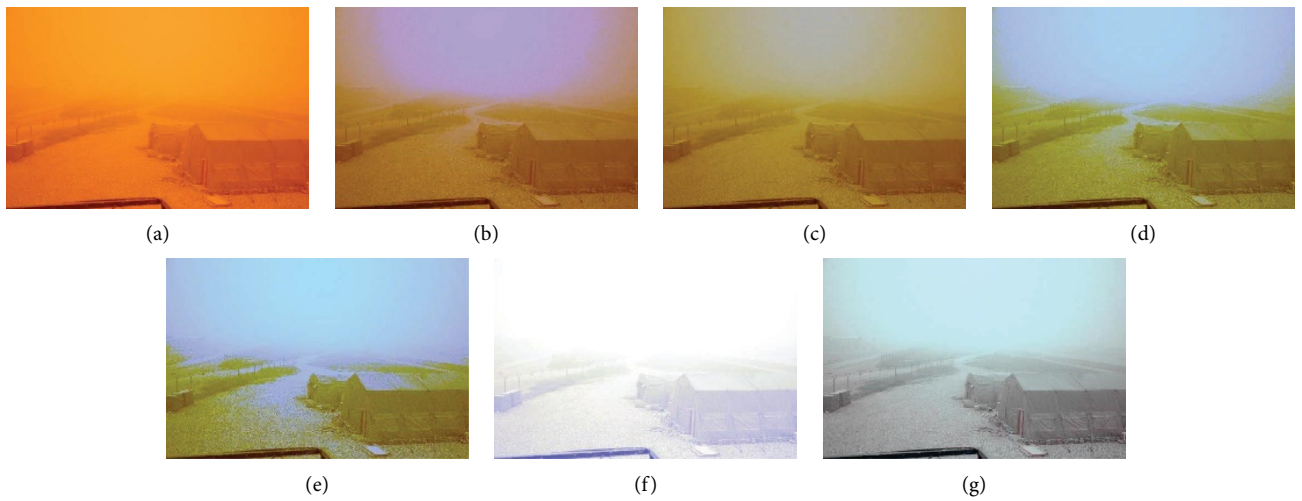

Figure 8: Performance comparison of different color correction algorithms. (a) Sand-dust image, (b) Gray Edge [34], (c) Max RGB [36], (d) Shades of Gray [35], (e) Gray-World [33], (f) OTM [16], and (g) Our.

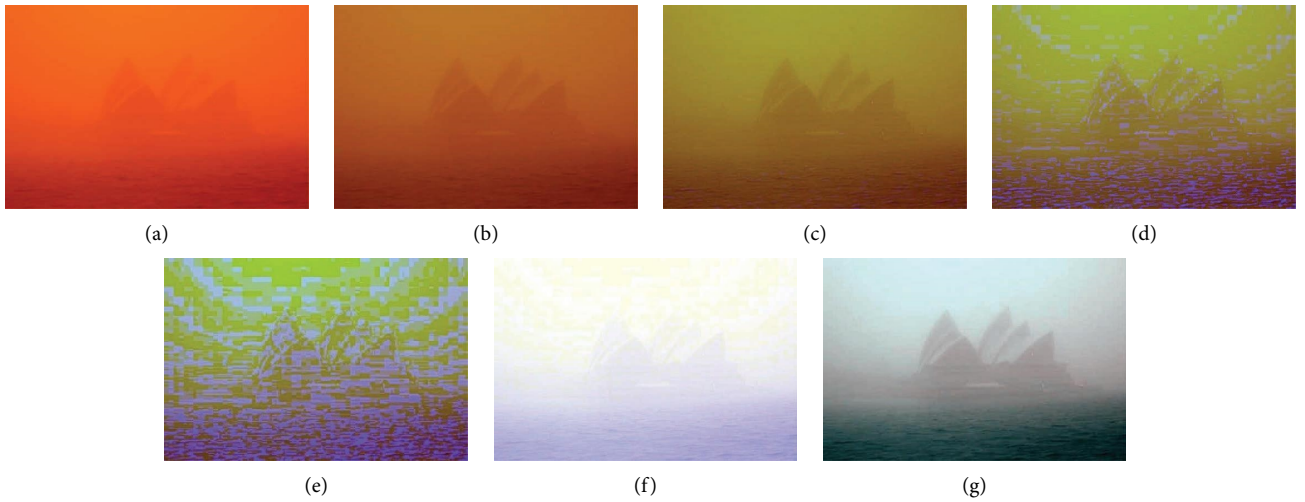

Figure 9: Performance comparison of different color correction algorithms. (a) Sand-dust image, (b) Gray Edge [34], (c) Max RGB [36], (d) Shades of Gray [35], (e) Gray-World [33]. (f) OTM [16], and (g) Our.

algorithms cannot manage severe sand-dust images and suffer from color distortions. SES [11] produces a lot of noise but also enhances details. Our method recovers clear details and has better visibility, and the resulting image quality is markedly better than those of the other methods.

4.4. Quantitative Evaluation

4.4.1. Quantitative Evaluation of Color Correction. Since there is no special evaluation index for color correction of sand-dust images, the quality of color correction cannot be quantitatively evaluated by indicators. We performed user studies to determine the quality of recovery by scoring the results of Gray Edge [34], Max RGB [36], Shades of Gray [35], Gray-World [33], OTM [16], and the proposed method. The score is between 1 and 5, with high scores indicating good results. We selected 10 experts with image processing experience and 10 colleagues without image processing experience to conduct user evaluation. The results processed by various algorithms are combined, and then, the user scores them; however, the user does not know the corresponding algorithm during the evaluation process. We report the average scores of 20 people on 100 sand-dust images in Figure 12.

Figure 12 shows that the proposed method obtained the highest score, predicting that it has better color recovery.

4.4.2. Quantitative Evaluation of the Sand-Dust Image Enhancement Effect. The lack of ground truth images makes the reference metrics PSNR and SSIM unusable. The literature [23] explored the nonreference metrics spatial-spectral entropy-based quality SSEQ [41] and blind image quality index BIQI [42] to evaluate the sand-dust images and proved their validity. In this study, we used these two metrics to

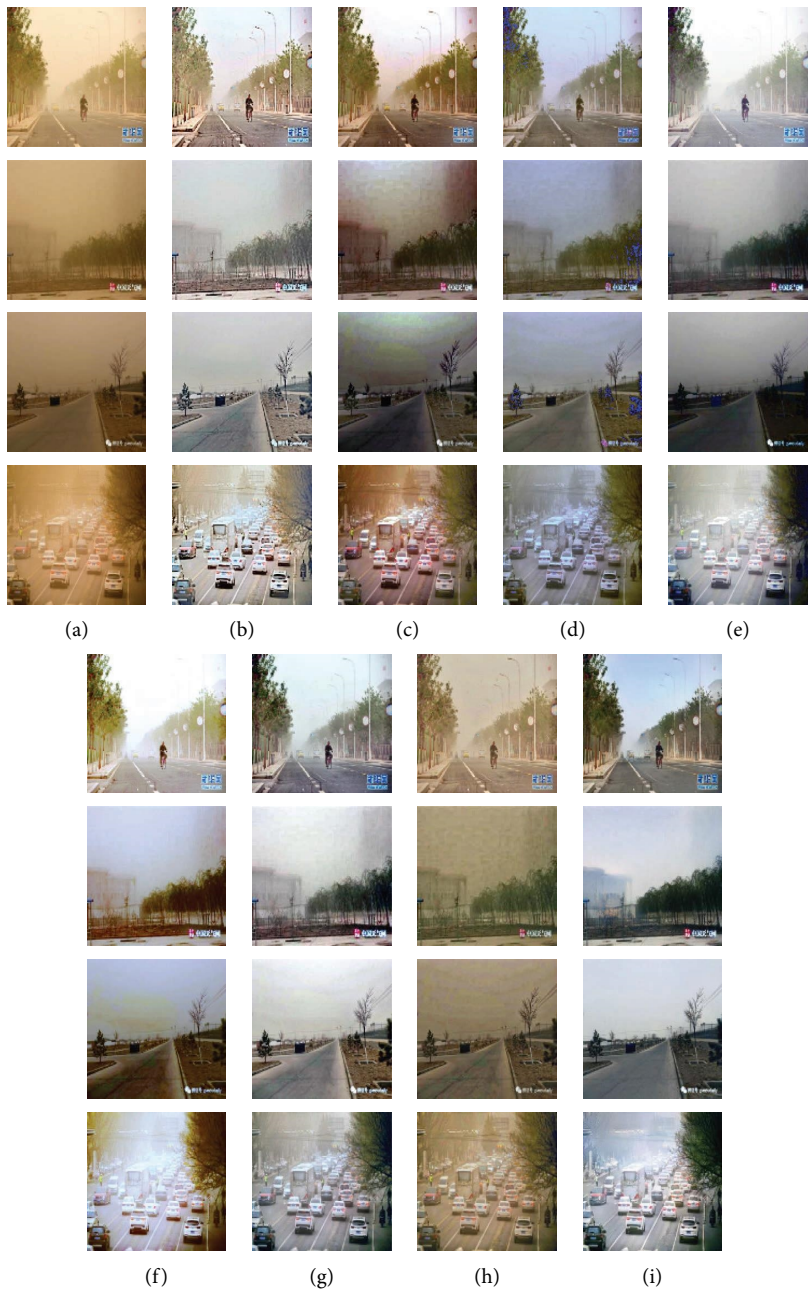

FIGURE 10: Qualitative comparison results: (a) sand-dust images, (b) RDCP [18], (c) CC [15], (d) FSS [14], (e) VR [16], (f) RBCP [13], (g) SES [11], (h) AOP [17], and (i) Ours.

evaluate the image quality on the test set, and the smaller their values, the better the image. In addition, we used the Fréchet inception distance (FID) [40] and average gradient (AG) [43] to measure the perceptual quality and the average gradient. The smaller the FID value is, the better the image, and the larger the AG value is, the better the image. From Table 1, the quantitative results indicate that the proposed algorithm is superior to other algorithms except RDCP [18]. In particular, for RDCP [18], its metrics SSEQ and AG are higher than those of the proposed algorithm, showing that RDCP [18] has a higher average gradient and contrast, but the improvement of this metric sacrifices the perceptual quality of the image. From the perceptual distance FID of RDCP [18], its value is markedly higher than that of the proposed algorithm. Combined with Figures 10 and 11(b), we can also see that the perceptual quality of RDCP [18] is low. These results thus show that the proposed unsupervised generative adversarial network has great advantages with regard to image quality.

4.5. Ablation Studies. To verify the effectiveness of the proposed model, we performed three groups of ablation studies on the test set: (1) validation of the proposed two-step

Figure 11: Qualitative comparison results: (a) sand-dust images, (b) RDCP [18], (c) CC [15], (d) FSS [14], (e) VR [16], (f) RBCP [13], (g) SES [11], (h) AOP [17], and (i) Ours.

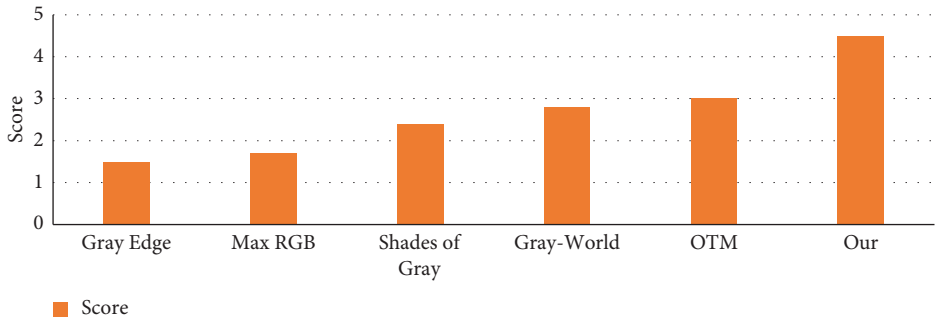

Figure 12: User scores.

Table 1: Average quantitative metric values.

	SSEQ↓	BIQI↓	FID↓	AG↑
RDCP	13.32	27.13	180.84	9.13
CC	16.72	27.22	188.26	5.79
FSS	14.87	25.22	210.08	5.86
VR	18.56	25.47	181.88	5.01
RBCP	18.05	24.85	191.68	6.00
SES	14.80	24.20	176.55	6.52
AOP	15.57	26.03	183.74	5.36
Ours	14.25	20.34	158.16	6.38

strategy; (2) validation of the proposed color correction strategy; and (3) validation of the unsupervised detail refinement network module component. The details of the ablation experiments are given as follows.

4.5.1. Validation of the Effectiveness of the Proposed Two-step Strategy. The proposed two-step strategy includes a color correction model in the first step and network refinement in detail in the second step. To verify the effectiveness of the two-step strategy, we perform the following ablation experiments: (1) color correction and (2) color correction plus detail refinement network. The objective metrics are shown in Table 2.

Table 2 shows that after the first step of color correction, SSEQ, BIQI, and FID decreased by 1.02, 1.44, and 7.11, respectively, and AG improved by 0.65 compared to the sand-dust image. The image quality is improved. After the second step of the detail refinement network, the SSEQ, BIQI, and FID decreased by 8.56, 5.22, and 21.04, respectively, compared with the results of the first step, and the AG improved by 2.90 compared with the results of the first step. Image quality improved markedly after the second step of detail refinement of the network. The visualization results are shown in Figure 13.

Figure 13(b) shows that, after color correction, the color shift has been sufficient removed. As shown in Figure 13(c), after the detail refinement network, the detail and clarity of the image are markedly improved, and the image has better visibility. Therefore, the effectiveness of the proposed two-step strategy at enhancing sand-dust images is demonstrated in terms of both objective metrics and subjective effects.

4.5.2. Ablation Experiments of the Effectiveness of the Proposed Color Correction Strategy. We design a color correction strategy, that is, red-green channel stretch-compensation-blue channel stretch-color shift removal. To prove its effectiveness, we conduct the following ablation experiments. First, the red-green channel stretching operation is removed, and the other operations remain unchanged. In this experiment, the remove red-green channel stretching operation in this study includes three experiments: one is to remove only the red channel stretching operation, one is to remove only the green channel stretch, and the other is to remove both the red-green channel stretch. Second, we remove the compensation operation, and other operations remain unchanged. Third, the blue channel stretching operation is removed, and the other operations remain unchanged. Fourth, the color shift correction factor is removed, and other operations remain unchanged. Experimental results are shown in Figure 14. Compared with the complete model, Figure 14(b) shows a slight color deviation without red channel stretching, and some details of the image are dark. As shown in Figures 14(c) and 14(d), when there is no green channel stretching or red-green channel stretching, serious color distortion occurs. Figure 14(e) shows that no compensation operation results in blue artifacts. As shown in Figure 14(f), no blue channel stretching causes the image to turn yellow. As shown in Figure 14(g), no color shift factor operation will cause slight dust or distortion. Therefore, each operation of the proposed strategy is necessary, and its effectiveness is proven.

Table 2: Average metric values for different components.

	SSEQ↓	BIQI↓	FID↓	AG↑
Input	23.83	27.00	186.31	2.83
a	22.81	25.56	179.20	3.48
b	14.25	20.34	158.16	6.38

To more comprehensively evaluate the effectiveness of color correction strategy, we give the user study scores for the different operations, taken in the same way as in section 4.4.1. The user study scores are shown in Figure 15. No red channel, no green channel, no red-green channel, no color compensation, no blue channel, no color shift, and completed in Figure 15 correspond to operations (b)–(h) in Figure 14, respectively. From Figure 15, the complete color correction algorithm has a higher score, which shows that each operation of the proposed strategy is beneficial to the improvement of color correction, and proves its effectiveness.

4.5.3. Ablation Experiments of the Proposed Components in the Unsupervised Detail Refinement Network. In the unsupervised detail refinement network, we primarily verify the impact of the proposed detail enhancement branch, the proposed coarse-grained discriminator and fine-grained discriminator, and the multiscale perception function on the network. To verify the effect of these components, we conduct the following ablation experiments: (1) no D: we remove the detail enhancement branch, and the other components remain unchanged; (2) no C: we remove the coarse-grained discriminator, and the other components remain unchanged; (3) no F: we remove the fine-grained discriminator, and the other components remain unchanged; (4) no L_P: we remove multiscale perception loss, and other components remain unchanged; and (5) the complete proposed model. The objective metrics are shown in Table 3. Except for no L_P, the complete model performs best compared to the other models in terms of metrics, which demonstrates the effectiveness of the proposed

(a) (b) (c)

Figure 13: Two-step effect images of our method: (a) sand-dust images, (b) results of color correction, and (c) results of detail refinement network.

components. In particular, for no L_P, the metrics SSEQ, BIQI, and AG are shown to be better than those of the complete model when the multiscale perceptual loss is removed. Considering the subjective appearance of Figure 16(e), the image is shown to be severely distorted, including many false images and nonexistent details, and leading to the abnormality and failure of these metrics SSEQ, BIQI, and AG. However, the perceptual quality of the image is low. As shown in the FID metric, the complete model performs better with no perceptual loss, which also shows the important role of multiscale perceptual loss. Based on the subjective appearance of Figure 16, the complete model includes more detailed information and better visibility and thus performs better than the other models. Therefore, the effectiveness of the proposed components is demonstrated by both subjective and objective comparisons.

4.6. Run Time. We report the average running time of each algorithm on the test set. All models are executed on the same configuration, and results are shown in Table 4. Because the other algorithms are relatively simple traditional methods, the running time is short, while the proposed algorithm is a neural network, and the running time is long but is similar to that of RDCP [18]. The average time of processing image size $256 * 256$ is less than 1 second, which does not significantly limit practical applications.

4.7. Other Applications

4.7.1. Application 1: Enhancement of Underwater Images and Haze Images. Figures 17 and 18 demonstrate that the method also has a good enhancement effect on haze images and underwater images, reflecting a good application scalability.

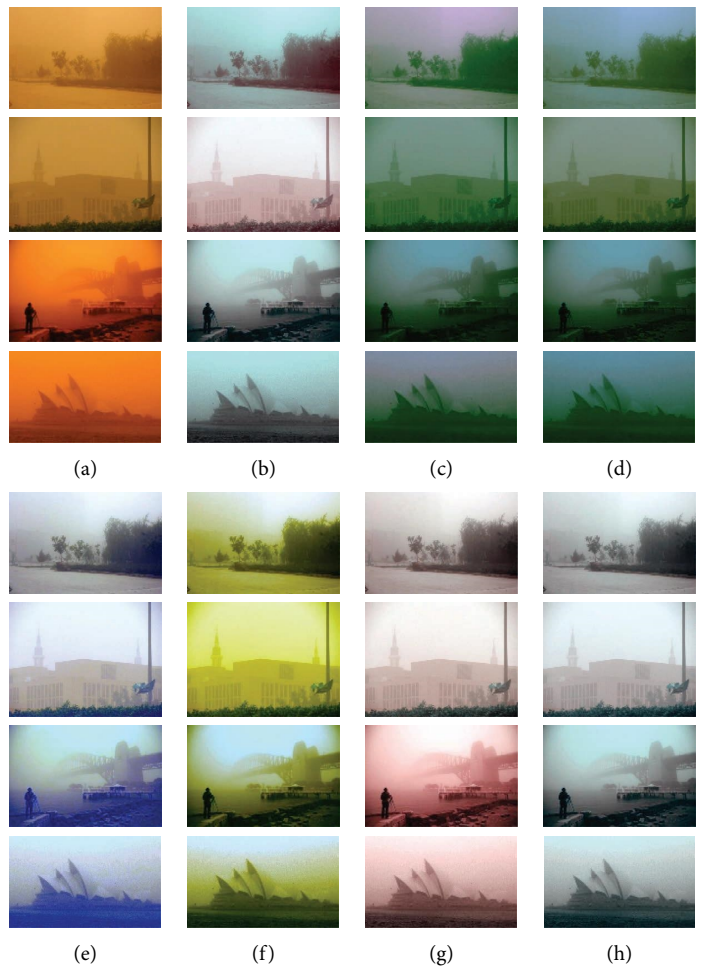

Figure 14: Effectiveness of the proposed color correction strategy: (a) sand-dust images, (b) no red channel stretching operation, (c) no green channel stretching operation, (d) no red-green channel stretching operation, (e) no color compensation operation, (f) no blue channel stretching channel operation, (g) no color shift factor operation, and (h) complete color correction algorithm.

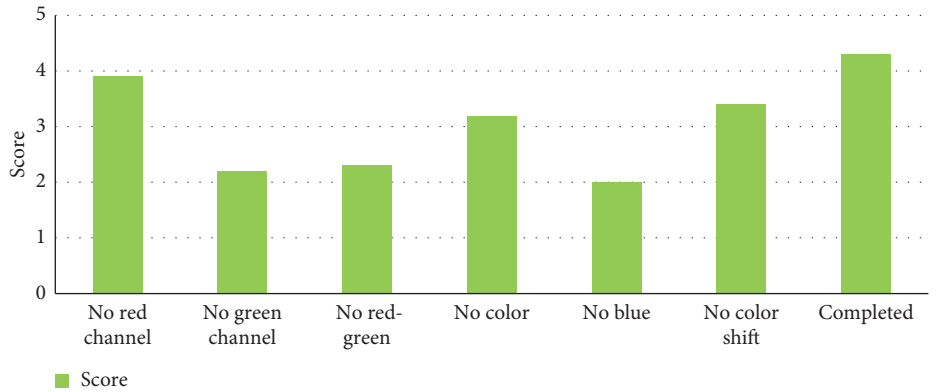

Figure 15: User study scores for different operations.

Table 3: Average metric values for different components.

	SSEQ↓	BIQI↓	FID↓	AG↑
No D	14.74	21.19	162.24	6.12
No C	17.61	23.10	173.74	4.81
No F	14.66	20.89	163.37	5.73
No L_p	11.16	19.55	178.92	8.25
Ours	14.25	20.34	158.16	6.38

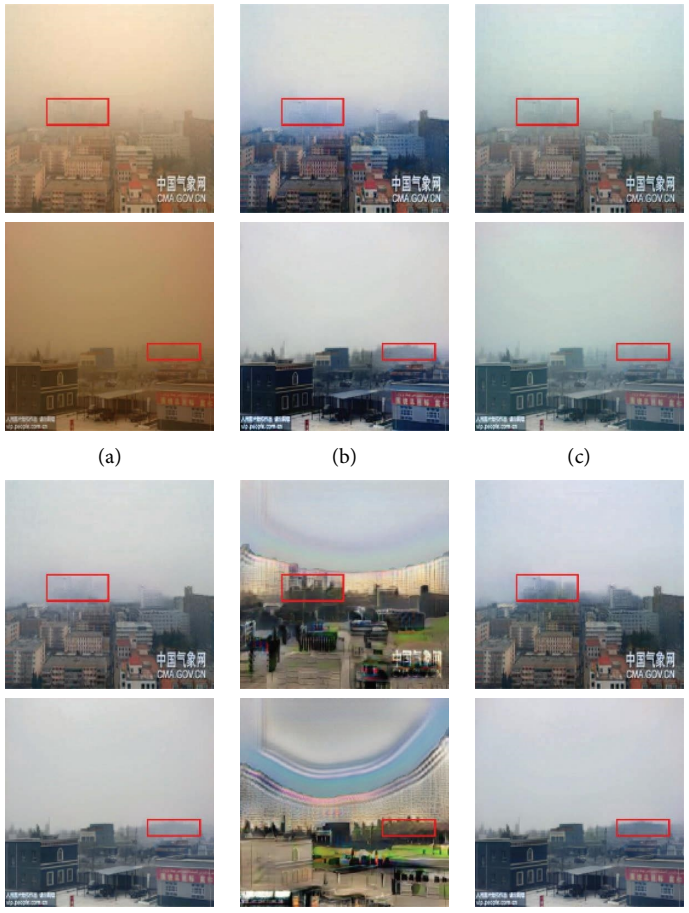

(a) (b) (c) (d) (e) (f)

Figure 16: Impact of different components on network performance: (a) sand-dust images, (b) no D, (c) no C, (d) no F, (e) no L_P, and (f) ours.

Table 4: The average running time of each algorithm.

Methods	Platform	Time (seconds)
RDCP	MATLAB/CPU	0.756
CC	MATLAB/CPU	0.132
FSS	Python/CPU	0.059
VR	MATLAB/CPU	0.165
RBCP	MATLAB/CPU	0.190
SES	Python/CPU	0.258
AOP	MATLAB/CPU	0.168
Proposed	MATLAB + Pytorch/CPU	0.848

4.7.2. Application 2: Application of Impact on Target Detection. Figure 19 shows that more targets can be detected in the enhanced image using the target detection Ssd algorithm [44], which also improves the detection capability and accuracy of the targets. The proposed algorithm promotes the application of advanced tasks well.

4.8. Failure Cases. The proposed algorithm does not perform well with some seriously degraded images. Color distortion and halo are introduced during enhancement in Figure 20. The reason for these results is that sand-dust occurs at night, and severe sand-dust weather increases the difficulty of removing sand from the image. The proposed method has

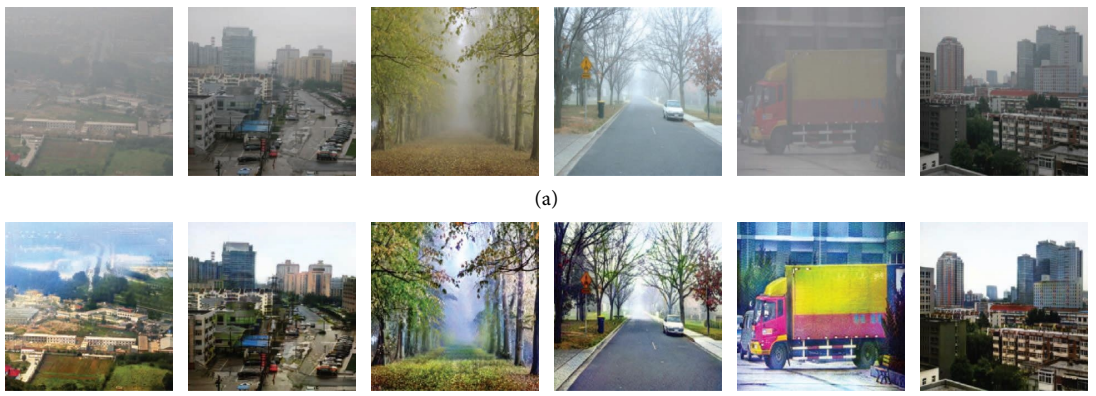

(a)

(b)

Figure 17: Examples of haze images enhancement: (a) haze images and (b) the dehazing results.

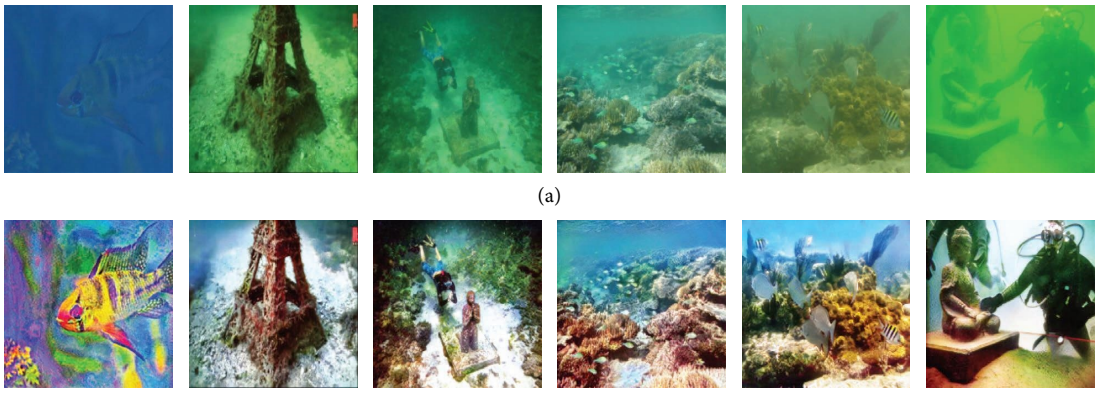

(a)

(b)

Figure 18: Examples of underwater images enhancement: (a) underwater images and (b) underwater images enhancement results.

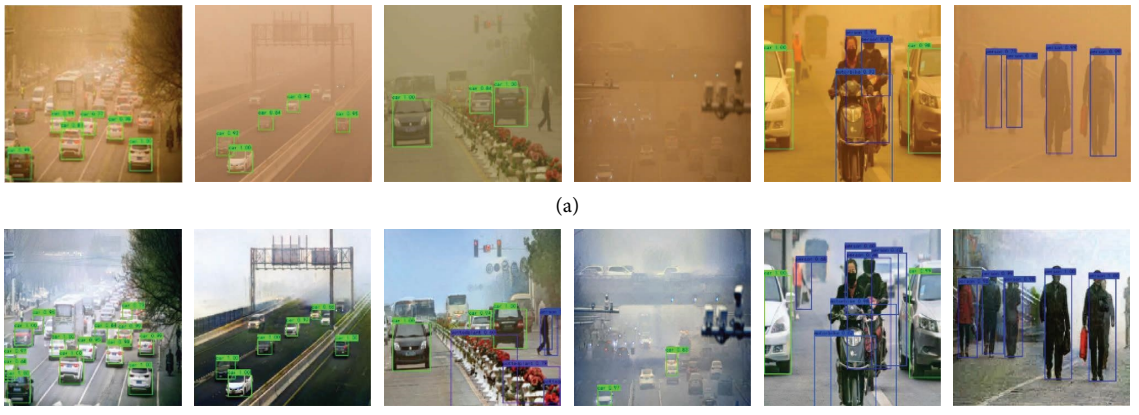

(a)

(b)

Figure 19: Impact on target detection: (a) target detection of sand-dust images and (b) target detection after enhancement.

(a) (b)

Figure 20: The failure cases: (a) sand-dust images and (b) results of our method.

insufficient constraints on unsupervised image enhancement, which is also a cause of image distortion.

5. Conclusion

In this paper, we propose a two-step unsupervised SIE method. In the first step, a color correction method based on linear stretching, blue channel compensation, and color shift correction factor removal is proposed. In the second step, an unsupervised detail refinement network restores the details well. The network reduces information loss by designing a detail enhancement branch, and the constructed coarse-grained and fine-grained discriminators guide the generator to generate more details. The introduced multiscale perception function promotes image fidelity. Experiments show that the method has good visibility with natural colors and clear details and thus outperforms existing methods.

Data Availability

The data supporting the current study are available from the corresponding author upon request.

Conflicts of Interest

The authors declare that they have no conflicts of interest.

Acknowledgments

This work was supported by the National Natural Science Foundation of China under Grant U1903213 and Xinjiang University Innovation Project (XJU2022BS071).

References

[1] C. Sakaridis, D. Dai, and L. Van Gool, "ACDC: the adverse conditions dataset with correspondences for semantic driving scene understanding," in *Proceedings of the IEEE/CVF International Conference on Computer Vision*, pp. 10765–10775, Montreal, Canada, June 2021.

[2] M. Bansal, M. Kumar, M. Kumar, and K. Kumar, "An efficient technique for object recognition using Shi-Tomasi corner detection algorithm," *Soft Computing*, vol. 25, no. 6, pp. 4423–4432, 2021.

[3] K. Rezaee, S. M. Rezakhani, M. R. Khosravi, and M. K. Moghimi, "A survey on deep learning-based real-time crowd anomaly detection for secure distributed video surveillance," *Personal and Ubiquitous Computing*, pp. 1–17, 2021.

[4] J. Y. Zhu, T. Park, P. Isola, and A. A. Efros, "Unpaired image-to-image translation using cycle-consistent adversarial networks," in *Proceedings of the IEEE International Conference on Computer Vision*, pp. 2223–2232, Venice, Italy, October 2017.

[5] W. Liu, X. Hou, J. Duan, and G. Qiu, "End-to-end single image fog removal using enhanced cycle consistent adversarial networks," *IEEE Transactions on Image Processing*, vol. 29, pp. 7819–7833, 2020.

[6] N. H. Kaplan, "Real-world image dehazing with improved joint enhancement and exposure fusion," *Journal of Visual Communication and Image Representation*, vol. 90, Article ID 103720, 2023.

[7] W. Wang, Z. Chen, and X. Yuan, "Simple low-light image enhancement based on Weber–Fechner law in logarithmic space," *Signal Processing: Image Communication*, vol. 106, Article ID 116742, 2022.

[8] Z. Al-Ameen, "Visibility enhancement for images captured in dusty weather via tuned tri-threshold fuzzy intensification operators," *International Journal of Intelligent Systems and Applications*, vol. 8, no. 8, pp. 10–17, 2016.

[9] X. Fu, Y. Huang, D. Zeng, X. P. Zhang, and X. Ding, "A fusion-based enhancing approach for single sandstorm image," in *Proceedings of the 2014 IEEE 16th International Workshop on Multimedia Signal Processing (MMSP)*, pp. 1–5, IEEE, Jakarta, Indonesia, September 2014.

[10] G. X. Gao, H. C. Lai, Y. Q. Liu, L. J. Wang, and Z. H. Jia, "Sandstorm image enhancement based on YUV space," *Optik*, vol. 226, Article ID 165659, 2021.

[11] T. H. Park and I. K. Eom, "Sand-dust image enhancement using successive color balance with coincident chromatic histogram," *IEEE Access*, vol. 9, pp. 19749–19760, 2021.

[12] G. Xu, X. Wang, and X. Xu, "Single image enhancement in sandstorm weather via tensor least square," *IEEE/CAA Journal of Automatica Sinica*, vol. 7, no. 6, pp. 1649–1661, 2020.

[13] G. Gao, H. Lai, Z. Jia, Y. Liu, and Y. Wang, "Sand-dust image restoration based on reversing the Blue Channel prior," *IEEE Photonics Journal*, vol. 12, no. 2, pp. 1–16, 2020.

[14] S. E. Kim, T. H. Park, and I. K. Eom, "Fast single image dehazing using saturation based transmission map estimation," *IEEE Transactions on Image Processing*, vol. 29, pp. 1985–1998, 2020.

[15] S. K. Dhara, M. Roy, D. Sen, and P. K. Biswas, "Color cast dependent image dehazing via adaptive airlight refinement and non-linear color balancing," *IEEE Transactions on*

Circuits and Systems for Video Technology, vol. 31, no. 5, pp. 2076–2081, 2020.

[16] Y. Yang, C. Zhang, L. Liu, G. Chen, and H. Yue, "Visibility restoration of single image captured in dust and haze weather conditions," *Multidimensional Systems and Signal Processing*, vol. 31, no. 2, pp. 619–633, 2020.

[17] A. Bartani, A. Abdollahpouri, M. Ramezani, and F. A. Tab, "An adaptive optic-physic based dust removal method using optimized air-light and transfer function," *Multimedia Tools and Applications*, vol. 81, no. 23, pp. 33823–33849, 2022.

[18] Z. Shi, Y. Feng, M. Zhao, E. Zhang, and L. He, "Let you see in sand dust weather: a method based on halo-reduced dark channel prior dehazing for sand-dust image enhancement," *IEEE Access*, vol. 7, pp. 116722–116733, 2019.

[19] H. Wu, Y. Qu, and S. Lin, "Contrastive learning for compact single image dehazing," in *Proceedings of the IEEE/CVF Conference on Computer Vision and Pattern Recognition*, pp. 10551–10560, Washington, DC, USA, August 2021.

[20] M. Hong, Y. Xie, C. Li, and Y. Qu, "Distilling image dehazing with heterogeneous task imitation," in *Proceedings of the IEEE/CVF Conference on Computer Vision and Pattern Recognition*, pp. 3462–3471, Seattle, WA, USA, June 2020.

[21] M. Wang, C. Li, and F. Ke, "Recurrent multi-level residual and global attention network for single image deraining," *Neural Computing & Applications*, vol. 35, no. 5, pp. 3697–3708, 2023.

[22] H. Huang, W. Yang, Y. Hu, J. Liu, and L. Y. Duan, "Towards low light enhancement with raw images," *IEEE Transactions on Image Processing*, vol. 31, pp. 1391–1405, 2022.

[23] Y. Si, F. Yang, Y. Guo, W. Zhang, and Y. Yang, "A comprehensive benchmark analysis for sand dust image reconstruction," *Journal of Visual Communication and Image Representation*, vol. 89, Article ID 103638, 2022.

[24] J. Huang, H. Xu, G. Liu, C. Wang, Z. Hu, and Z. Li, "SIDNet: a single image dedusting network with color cast correction," *Signal Processing*, vol. 199, Article ID 108612, 2022.

[25] J. Huang, Z. Li, C. Wang, Z. Yu, and X. Cao, "FFNet: a simple image dedusting network with feature fusion," *Concurrency and Computation: Practice and Experience*, vol. 33, no. 24, Article ID e6462, 2021.

[26] P. Liang, P. Dong, F. Wang et al., "Learning to remove sandstorm for image enhancement," *The Visual Computer*, vol. 39, no. 5, pp. 1829–1852, 2022.

[27] B. Lu, J. C. Chen, and R. Chellappa, "Unsupervised domain-specific deblurring via disentangled representations," in *Proceedings of the IEEE/CVF Conference on Computer Vision and Pattern Recognition*, pp. 10225–10234, Long Beach, CA, USA, June 2019.

[28] W. Du, H. Chen, and H. Yang, "Learning invariant representation for unsupervised image restoration," in *Proceedings of the IEEE/CVF Conference on Computer Vision and Pattern Recognition*, pp. 14483–14492, Seattle, WA, USA, June 2020.

[29] H. Sun, Y. Zhang, P. Chen et al., "Scale-free heterogeneous cycleGAN for defogging from a single image for autonomous driving in fog," *Neural Computing & Applications*, vol. 35, no. 5, pp. 3737–3751, 2021.

[30] Y. Wei, Z. Zhang, Y. Wang et al., "Deraincyclegan: rain attentive cyclegan for single image deraining and rainmaking," *IEEE Transactions on Image Processing*, vol. 30, pp. 4788–4801, 2021.

[31] Z. Ni, W. Yang, S. Wang, L. Ma, and S. Kwong, "Towards unsupervised deep image enhancement with generative adversarial network," *IEEE Transactions on Image Processing*, vol. 29, pp. 9140–9151, 2020.

[32] Y. Jiang, X. Gong, D. Liu et al., "Enlightengan: deep light enhancement without paired supervision," *IEEE Transactions on Image Processing*, vol. 30, pp. 2340–2349, 2021.

[33] G. Buchsbaum, "A spatial processor model for object colour perception," *Journal of the Franklin Institute*, vol. 310, no. 1, pp. 1–26, 1980.

[34] J. Van De Weijer, T. Gevers, and A. Gijsenij, "Edge-based color constancy," *IEEE Transactions on Image Processing*, vol. 16, no. 9, pp. 2207–2214, 2007.

[35] G. D. Finlayson and E. Trezzi, "Shades of gray and colour constancy," in *Proceedings of the Color and Imaging Conference*, pp. 37–41, Society for Imaging Science and Technology, Springfield, VA, USA, July 2004.

[36] E. H. Land, "The retinex theory of color vision," *Scientific American*, vol. 237, no. 6, pp. 108–128, 1977.

[37] T. Miyato, T. Kataoka, M. Koyama, and Y. Yoshida, *Spectral Normalization for Generative Adversarial Networks*, 2018, https://arxiv.org/abs/1802.05957.

[38] X. Mao, Q. Li, H. Xie, R. Y. K. Lau, Z. Wang, and S. Paul Smolley, "Least squares generative adversarial networks," in *Proceedings of the IEEE International Conference on Computer Vision*, pp. 2794–2802, Cambridge, MA, USA, June 2017.

[39] K. Simonyan and A. Zisserman, "Very deep convolutional networks for large-scale image recognition," 2014, https://arxiv.org/abs/1409.1556.

[40] M. Heusel, H. Ramsauer, T. Unterthiner, B. Nessler, and S. Hochreiter, "Gans trained by a two time-scale update rule converge to a local nash equilibrium," *Advances in Neural Information Processing Systems*, vol. 30, pp. 6629–6640, 2017.

[41] L. Liu, B. Liu, H. Huang, and A. C. Bovik, "No-reference image quality assessment based on spatial and spectral entropies," *Signal Processing: Image Communication*, vol. 29, no. 8, pp. 856–863, 2014.

[42] A. K. Moorthy and A. C. Bovik, "A modular framework for constructing blind universal quality indices," *IEEE Signal Processing Letters*, vol. 17, p. 7, 2009.

[43] W. Zhang, L. Dong, X. Pan, J. Zhou, L. Qin, and W. Xu, "Single image defogging based on multi-channel convolutional MSRCR," *IEEE Access*, vol. 7, pp. 72492–72504, 2019.

[44] W. Liu, D. Anguelov, and D. Erhan, "Ssd: single shot multibox detector," in *Proceedings of the European Conference on Computer Vision*, pp. 21–37, Springer, Paris, France, July 2016.